Actin Protofilament Orientation in Deformation of the Erythrocyte Membrane Skeleton

Catherine Picart, Paul Dalhaimer, and Dennis E. Discher
Institute for Medicine and Engineering, and School of Engineering and Applied Science, University of Pennsylvania, Philadelphia, Pennsylvania 19104 USA

ABSTRACT The red cell's spectrin-actin network is known to sustain local states of shear, dilation, and condensation, and yet the short actin filaments are found to maintain membrane-tangent and near-random azimuthal orientations. When calibrated with polarization results for single actin filaments, imaging of micropipette-deformed red cell ghosts has allowed an assessment of actin orientations and possible reorientations in the network. At the hemispherical cap of the aspirated projection, where the network can be dilated severalfold, filaments have the same membrane-tangent orientation as on a relatively unstrained portion of membrane. Likewise, over the length of the network projection pulled into the micropipette, where the network is strongly sheared in axial extension and circumferential contraction, actin maintains its tangent orientation and is only very weakly aligned with network extension. Similar results are found for the integral membrane protein Band 3. Allowing for thermal fluctuations, we deduce a bound for the effective coupling constant, α, between network shear and azimuthal orientation of the protofilament. The finding that α must be about an order of magnitude or more below its tight-coupling value illustrates how nanostructural kinematics can decouple from more macroscopic responses. Monte Carlo simulations of spectrin-actin networks at ~10-nm resolution further support this conclusion and substantiate an image of protofilaments as elements of a high-temperature spin glass.

INTRODUCTION

In addition to its role in cytoplasmic structuring, F-actin is a ubiquitous component at cell membranes. Even the red cell membrane's relatively simple spectrin network appears critically dependent on short, stiff actin protofilaments (~14 ± 1 subunits). In the red cell, F-actin forms junctional nodes cross-linked and intertriangulated by more flexible spectrin chains (Fig. 1) (Bennett and Stenbuck, 1979; Byers and Branton, 1985; Shen et al., 1986; Reid et al., 1990; Alloisio et al., 1993; Ursitti and Fowler, 1994). This structure is of general importance to erythrocyte function, as evident from the component defects and deficiencies that lead to easily fragmentable membranes and anemias of varying severity (e.g., Waugh and Agre, 1988; Mohandas and Evans, 1994; Discher et al., 1995). To further elucidate determinants of network structure, fluorescence polarization microscopy (FPM) (Axelrod, 1979; Zhukarev et al., 1995) has recently been applied to resealed erythrocyte ghosts harboring rhodamine-phalloidin-labeled actin (Picart and Discher, 1999). By use of FPM methods, actin protofilaments in discocytes and osmotically sphered ghosts were shown to be essentially tangent to the membrane, at least within the 15°–20° resolution of current methods. The results also appeared most consistent with a random azimuthal angle, η (Fig. 1 *A*), leading to some speculation as to whether this intrinsic orientational parameter might be physically influenced by deformation of the membrane.

Filament orientation is an issue of broad cell biological relevance, inasmuch as filamentous actin is found in various states of order at or near the membranes of many deformable, eukaryotic cells. A couple of examples beyond the erythrocyte are worth citing. Oriented growth of F-actin from specifically angled branching sites that involves the actin-binding protein Arp 2/3 (Mullins et al., 1998) is currently believed to drive the leading edge of motile cells. Wrapped around the circumference of the cylindrical outer hair cell, F-actin also directs the vectorial transduction of sound to sensory neurons (Holley and Ashmore, 1990; Oghalai et al., 1998). To address the general issue of mesoscale actin response in cell deformation, fluorescence polarization microscopy has been coupled to micropipette aspiration. A first application here is to rhodamine-phalloidin-labeled actin protofilaments in resealed erythrocyte ghosts.

The essential physical process in focus is illustrated in Fig. 1 *A*, where an initially undeformed portion of membrane network is distorted with spectrin chain extension as well as contraction. Network stretching of the magnitude sketched (twofold extension) certainly occurs along the cylindrical portion of the micropipette-aspirated projection, as originally conjectured by Evans (Evans, 1973; Evans and Skalak, 1980) and as directly supported by both fluorescence imaging (Discher and Mohandas, 1996) and more recent patterned photobleaching (Lee et al., 1999). Rotation of actin protofilaments would certainly seem intuitive in this process. More rigorously, because the protofilament length (Fowler, 1996) is orders of magnitude smaller than the persistence length of F-actin (Kas et al., 1996) while also

Received for publication 6 March 2000 and in final form 20 August 2000.

Address reprint requests to Dr. Dennis Discher, University of Pennsylvania, 112 Towne Building, Philadelphia, PA 19104-6315. Tel.: 215-898-4809; Fax: 215-573-6334; E-mail: discher@eniac.seas.upenn.edu.

Dr. Picart's present address is Ecole Européene de Chimie, Polymères, Matériaux, Strasbourg, France.

0006-3495/00/12/2987/14 $2.00

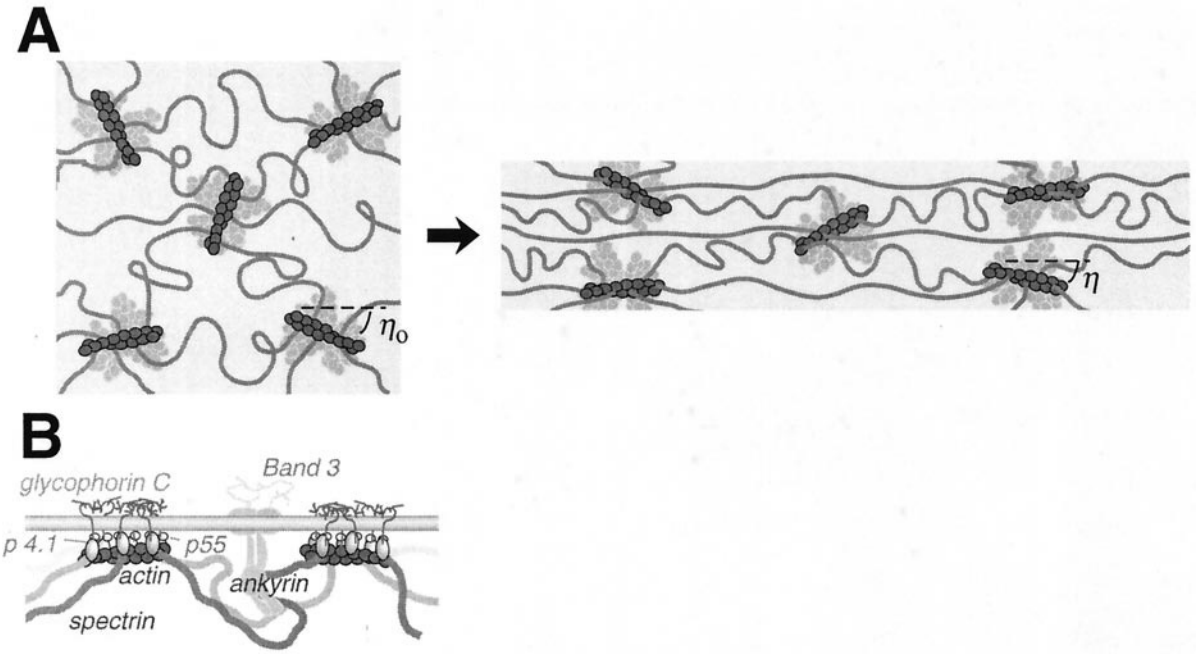

FIGURE 1 Scaled schematics of the red cell membrane's spectrin-actin network. (*A*) View from the inside of the cell, showing actin protofilaments lying tangent to the bilayer, randomly directed, and intertriangulated by spectrin (at *left*). The reversibly deformed state (at *right*) shows actin together with spectrin, either elongated or compressed. (*B*) Included in the side view are several integral and peripheral membrane proteins implicated in anchoring the actin protofilaments and spectrin to the overlying bilayer. Note that the helical actin protofilaments have lengths of ~35 nm and that the actin filaments are interconnected by spectrin with a spacing of ~75 nm, center to center. Spectrin tetramers are drawn as ~200-nm-long flexible elements.

being roughly twice the persistence length of spectrin (e.g., Discher et al., 1998), the protofilaments can be considered rigid compared to spectrin. Therefore, a given actin protofilament will not be extended, but its mean azimuthal angle might very well rotate from an initial value η_o to a new value η because of spectrin extension and lateral steric interactions. The fact that actin protofilaments are long relative to their spacing in situ suggests that any actin filament nanorotations would establish new "boundary conditions" on spectrin extension and thereby also contribute nontrivially to network elasticity. The end result could well be, however, a spin-glass system with counteracting elastic in place of magnetic spin interactions (e.g., Franzese, 2000).

Azimuthal fluctuations would complicate, but not necessarily invalidate, the static picture above. Of course, given that all the network components are in thermal motion at ~300 K, thermal averaging must apply, i.e., $\eta = \langle\eta\rangle$. However, it should be clear that the spectrin tethers and the associated finite shear rigidity preclude the actin protofilaments from spinning freely. A well-defined thermal average η should therefore emerge for each filament, with fluctuations being related to the network's shear rigidity through local tethering arrangements, couplings, and perhaps also spectrin unfolding (Rief et al., 1999). Whether rotations of actin are weakly or tightly coupled to overall network motions is among the central issues to be examined. Equally important to address is whether the tangent orientation of membrane actin presumed above is significantly disrupted by spectrin extension. Disruption is a particular possibility in curved regions of membrane where a membrane-normal component of force will arise.

The following Materials and Methods section briefly reviews details of the experimental methods, including a necessary summary of single-filament FPM results. Subsequently, a theoretical backdrop for FPM aspiration experiments is provided by elaboration of a zero-temperature, continuum hypothesis for actin filament reorientation in network deformation. The relatively simple affine, reorientation model concludes with predictions, plus or minus thermal fluctuations, for the magnitude of azimuthal reorientation of protofilaments in micropipette deformation. While instructive, the theoretical kinematics are then given an experimental context: FPM results are presented and discussed for red cell ghosts pulled into micropipettes to varying extents. Ultimately, the results prove consistent with 1) strong molecular constraints on actin's orientation but only with respect to the membrane, and 2) a surprisingly weak, almost neutral influence of deformation on azimuthal nanorotations of protofilaments.

MATERIALS AND METHODS

Fluorescence polarization microscope and micromanipulation

As described by Picart and Discher (1999), fluorescence image collection was accomplished through strain-free objectives on an infinity-corrected

Nikon TE-300 inverted microscope: either a 40× (1.0 NA) or a 60× (1.4 NA) objective was used, with an immersion oil of refractive index 1.52. A high-sensitivity, cooled and back-thinned CCD camera (CH360; Photometrics, Tucson, AZ); controlled by Image Pro (Silver Spring, MD) software running on a Pentium 200 MHz PC, was connected to the side port of the microscope via a 10× magnification lens. A Chroma Technology (Brattleboro, VT) filter set consisting of an exciter (HQ545/30), an emitter (HQ610/75), and a dichroic (Q565LP) was used for all imaging. Mounted between the microscope's 100-W Hg excitation lamp and the dichroic reflector was a three-holed slider with both vertically and horizontally oriented polarizers (Meadowlark Optics, Denver, CO). The excitation lamp was shuttered (Uniblitz from Vincent Associates, Rochester, NY) to synchronize excitation with a second shutter exposing the CCD; the typical exposure time was set between 200 and 300 ms. Mounted between the emission filter and the camera was a second three-holed slider. The micropipette manipulation system was analogous to that described previously (Discher et al., 1994; Lee et al., 1999). Furthermore, based on images of swollen ghosts held inside or outside of a micropipette, it does not appear that the micropipette wall detectably affects polarization imaging. All experiments were carried out at 23°C.

Where object symmetry permitted, image intensities were averaged for like polarizer orientations. However, to deal with the symmetry breaking by the micropipette, a laboratory-fixed coordinate frame is introduced, with z always in the direction of the micropipette axis and x along the optical axis. If both polarizers are parallel to the z axis, then the fluorescence intensity at a given point A in an image will be denoted by $F^{A}_{=}$. If both polarizers are perpendicular to the z axis, then the fluorescence intensity at point A will be denoted by $F^{A}_{\parallel}$. If the excitation polarizer is parallel to the z axis and the emission polarizer is perpendicular to the z axis, then the fluorescence intensity at the given point A will be denoted by $F^{A}_{\vdash}$. If the excitation polarizer is perpendicular to the z axis and the emission polarizer is parallel to the z axis, then the fluorescence intensity at the given point A will be denoted by $F^{A}_{\dashv}$. Actin protofilaments can, of course, be oriented in any direction with respect to these optically defined axes; a pixelated ensemble yields the signals just listed for point A. For single actin filaments, polarization intensity notation will conform to prior convention as described below and introduced by Picart and Discher (1999).

F-actin and EMA-band 3 labeling

Rhodamine phalloidin was purchased from Sigma (St. Louis, MO). Labeling of the red cell cytoskeletal network was achieved during reversible hemolysis as outlined in previous studies (Discher et al., 1994). Rabbit muscle G-actin was purchased as 99% pure in buffered solution from Cytoskeleton (Denver, CO) and stored frozen at −70°C. Polymerization and observation in deoxygenation buffer were also performed as described by Picart and Discher (1999). In brief, 10 mg/ml G-actin solution was diluted 1:100 into buffer A (300 mM KCl, 10 mM $MgCl_2$, 40 mM phosphate-buffered saline, 0.05 mM β-mercaptoethanol) that had been prediluted to 25% v/v with deionized water. After polymerization and filament collection by centrifugation, the pelleted F-actin was resuspended in buffer containing an oxygen depletion system (Kishino and Yanagida, 1988) of 2.3 mg/ml glucose, 0.018 mg/ml glucose oxidase, and 0.1 mg/ml catalase. The chamber for observation was assembled from a microscope slide typically coated with poly-L-lysine (0.01% w/v in water) to immobilize the filaments.

Band 3 was labeled with eosin-5-maleimide (EMA) (Molecular Probes, Eugene, OR) by methods described previously (Discher et al., 1994). In comparison to rhodamine-phalloidin-labeled membranes, EMA appeared much brighter initially but photobleached much more rapidly. Corrections were made as needed for photobleaching by taking multiple images and estimating the rate of signal decay.

Single-filament FPM

Emission intensities from single filaments were tabulated with respect to an optics-defined triad. As indicated for the image intensity surface of Fig. 2 *A*, X_1 is always set by the propagation or optical axis of the microscope. It always also coincides with the laboratory-fixed x direction. In contrast, X_3 is set by the excitation polarization and can coincide with either the laboratory-fixed y or z direction. Filament orientation is denoted in intensity measures with respect to this X_i frame by a presubscript. For example, ${}_{X2}I_{\parallel}$ denotes a polarization intensity for a filament lying parallel to the X_2 axis and imaged with the emission polarizer in the X_3 direction defined by the excitation polarizer. Filaments generally have an orientation in 3-space (Fig. 2 *A*, *inset*), however, with direction cosines in the optical frame, such as $N_{X1} = \cos \eta_{X1}$. Optical transfer functions that relate the intensity to filament orientation,

$$I_{\parallel} \approx \alpha_0 + \alpha_1 N^{p1}_{x1} + \alpha_2 N^{p2}_{x2} + \alpha_3 N^{p3}_{x3} \tag{1a}$$

$$I_{\perp} \approx \beta_0 + \beta_1 N^{p1}_{x1} + \beta_2 N^{p2}_{x2} + \beta_3 N^{p3}_{x3} \tag{1b}$$

are suggested by Axelrod (1979), who gave the idealized sets of (α_i, β_i) for an isolated dipole observed under high NA. For the isolated dipole, $p_i = 2$ for all i, and the constant terms vanish. Because $|\mathbf{N}| = 1$, however, it is equally reasonable to eliminate one N_{Xi} and keep the constant terms. For symmetry reasons, the X_2 term will be eliminated in what follows. Furthermore, Fig. 2 *A* as well as additional analyses, including that of Picart and Discher (1999), suggest that long filaments oriented normal to the plane are as intense as those in the plane; in particular, ${}_{X1}I_{\perp} \sim {}_{X2}I_{\perp} \sim {}_{X3}I_{\perp}$. Equation 1b thus reduces to a constant independent of **N** but reflective of experimental parameters such as fluorescent labeling, lamp intensity, alignment of polarizers, etc. Variations between experiments are therefore minimized by tabulating ratios of ($I_{\parallel}/I_{\perp}$), as reported by Picart and Discher (1999) and employed here in the forms

$$({}_{\eta X3}I_{\parallel}/{}_{\eta X3}I_{\perp}) \approx 1.0 + 1.4 \cos^{p} \eta_{X3} \tag{2a}$$

$$\langle ({}_{\eta X3}I_{\parallel}/{}_{\eta X3}I_{\perp}) \rangle_{\eta X3} \approx 1.39 \pm 0.13 \tag{2b}$$

$$({}_{X2}I_{\parallel}/{}_{X3}I_{\perp}) \approx ({}_{X2}I_{\parallel}/{}_{X2}I_{\perp}) \approx 1.0 \tag{2c}$$

$$({}_{X1}I_{\parallel}/{}_{X1}I_{\perp}) \approx 1.35 \pm 0.14 \tag{2d}$$

Note that the ratio $({}_{\eta X3}I_{\parallel}/{}_{\perp X3}I\perp)$ denotes an angle-dependent polarization ratio for a single filament in the X_2-X_3 plane (Fig. 2 *B*), whereas $\langle \ldots \rangle_{\eta X3}$ denotes an angle average obtained from a ratio of total image intensities for parallel and crossed polarizers. Both results are fit well with $p_3 = 4$. The latter, integrated constraint was largely ignored in the previous analyses of Picart and Discher (1999), where $p = 2$ was assumed. Based finally on all of the above, a single optical transfer function is approximated as

$$(I_{\parallel}/I_{\perp}) \approx a_0 + a_1 N^{p1}_{X1} + a_2 N^{p2}_{X2} + a_3 N^{p3}_{X3} \tag{2e}$$

where $a_0 = 1.0$, $a_1 = 0.35$, $a_2 = 0.0$, $a_3 = 1.4$, $p_1 = 4$, and $p_3 = 4$. The surface defined by a vector from the origin and of length ($I_{\parallel}/I\perp$) with direction specified by the angles η_{X1} and η_{X3} is shown in Fig. 2 *C*. Such a transfer function, it must be stressed, is instrument-specific, so that one must return more generally to Eq. 1 and determine suitable (α_i, β_i) while searching, if desired, for simplifying approximations.

THEORETICAL PRELIMINARIES

Affine rotation model

The Materials and Methods section above illustrates a general ability to quantify actin filament orientation and thus leads to the question, why might protofilament rotations be

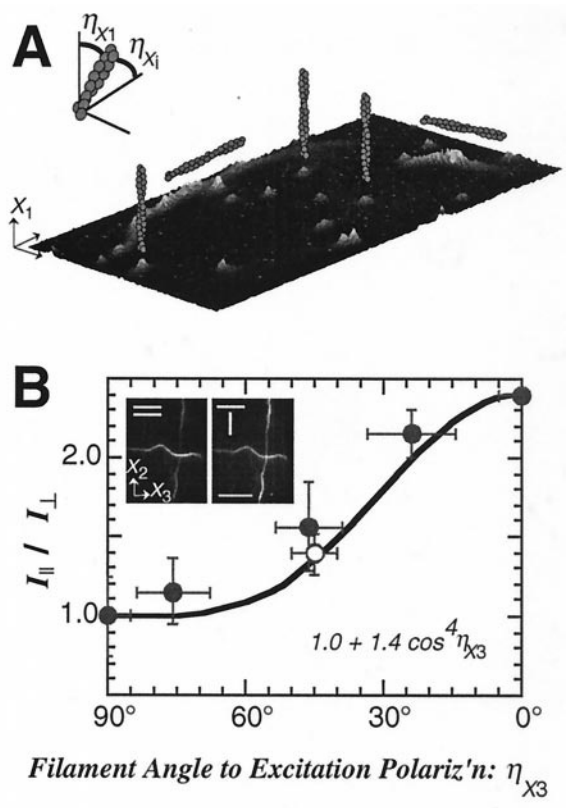

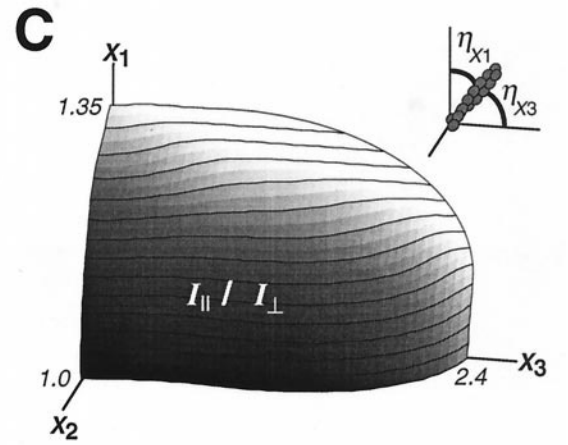

FIGURE 2 Actin filament intensities when oriented with respect to the optical X_i axes. (*A*) Image intensity surface, which shows that isolated filaments parallel to the optical axis (X_1) tend to be as bright as filaments in the X_2-X_3 plane. (*B*) Polarization ratios for individual actin filaments, or portions of filaments, oriented with respect to the excitation direction (X_3) (cumulated from Picart and Discher; 1999. All filaments (>30) were on or near the coverslip, in the X_2-X_3 plane, but oriented at an angle η_{X3} with respect to the X_3 direction. The open data point corresponds to Eq. 2b, which is an average obtained from intensity ratios of whole images. (*Inset*) Polarization images of individual actin filaments; excitation and emission polarizers are either parallel (*left*) or crossed (*right*). The scale bar is 5 μm. (*C*) Surface of a distorted unit sphere for filament polarization ratios (Eq. 2e).

anticipated in red cell aspiration? A "zero temperature" answer is based on the process illustrated in Fig. 3 *A*: a generic elastic sheet with a fan of painted line segments on it is geometrically transformed, variably extending and rotating segments of the fan in the process. The stretch factor λ_1 and lateral contraction λ_2 define an affine transformation that applies pointwise within the sheet. An initially uniform fan or distribution $P(\eta_o)$ (Fig. 3 *B*) of such line segments is clearly skewed nonuniformly by such a shearing distortion. The mapping, which we will denote by a tensor $\mathbf{\Gamma}$, where $\Gamma_{11} = \lambda_1$, $\Gamma_{22} = \lambda_2$, and $\Gamma_{12} = \Gamma_{21} = 0$, allows a straightforward solution for the relative rotation of material segments. For an initial line segment of length l_o with a direction denoted by the unit vector $\mathbf{M}$, the same line segment of new length l, in the deformed state, also has a new direction specified by $\mathbf{m}$. With these definitions, it can be shown that $\mathbf{m}\, l = \mathbf{\Gamma}\, \mathbf{M}\, l_o$. Thus, employing the unit vector components $(M_1, M_2) = (\cos \eta_o, \sin \eta_o)$ and $(m_1, m_2) = (\cos \eta_{affine}, \sin \eta_{affine})$, the new angle and corresponding segment extension can be solved for in terms of the original angle and the material transformation:

$$\cos \eta_{affine} = [(\lambda_1/\lambda_2)^2 \sin^2\eta_o + \cos^2\eta_o]^{-1/2} \cos \eta_o \qquad (3a)$$

$$l/l_o = [\lambda_2^2 \sin^2 \eta_o + \lambda_1^2 \cos^2\eta_o]^{1/2} \qquad (3b)$$

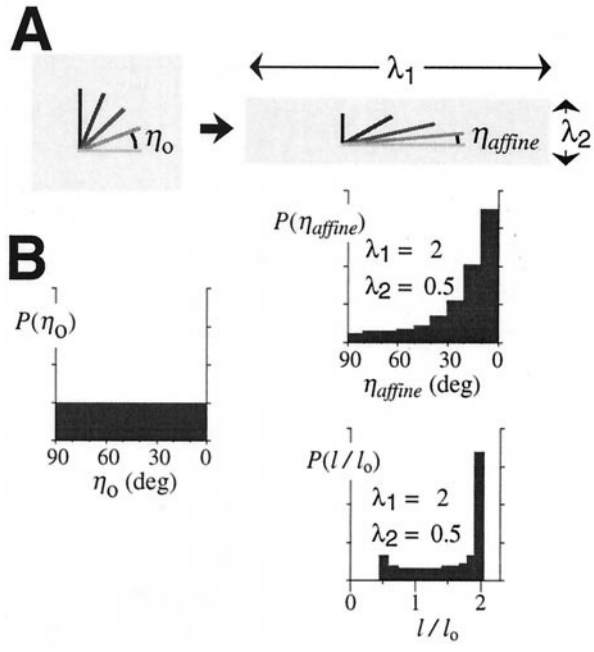

FIGURE 3 Skewing of material filaments in affine deformation of a continuum. (*A*) An initial fan of material lines that are painted on an undeformed portion of material is distorted in biaxial transformation to a deformed state. The *i*th material line has an initial angle η_o that rotates to a new angle η_{affine}. This occurs in a manner that depends nonlinearly on η_o. As a consequence, an initially random distribution of filament angles, shown at left in *B*, can be transformed to a nontrivial distribution of angles that is significantly skewed. In addition, the distribution of filament extensions is bimodal and is bounded by the extension ratios.

Equation 3a yields the appropriate trivial limits: $\eta_{affine} = 0°$ or 90° whenever $\eta_o = 0°$ or 90°, respectively; and $\eta_{affine} = \eta_o$ whenever $\lambda_1 = \lambda_2$. To illustrate the effects of affine rotation on a uniformly distributed fan of line segments, an experimentally relevant Γ has been assumed to calculate the $P(\eta_{affine})$ shown in Fig. 3 *B*. The skew of this distribution toward small angles reveals the propensity for material lines to align with the direction of principal deformation, the *1* axis here. The effect is one of shear alignment, with principal shear lines being rotated from the chosen *1*, *2* directions. Whether actin in a spectrin network rotates so much in such a deformation is the central issue to be addressed.

The material segment extension, l/l_o, given by Eq. 3b yields an asymmetrical, bimodal distribution $P(l/l_o)$ that is strictly bounded by peaks at λ_1 and λ_2, though skewed toward λ_1. This result coarsely resembles spectrin stretch distributions computed in Monte Carlo simulation of a triangulated network under micropipette aspiration (e.g., Fig. 7 *A*, Discher et al., 1998). Indeed, in relating the present affine model results to deformation of the spectrin-actin network, it seems most suitable to propose, as an initial framework, that actin protofilaments only rotate, whereas spectrin chains are changed in end-to-end length. Intuitively, this assumption should at least provide an upper bound on actin protofilament rotations. In addition, Eq. 3 implies that we need only know the local $\mathbf{\Gamma}$ to estimate actin reorientation. This proves fortunate because conventional fluorescence experiments (Fig. 4 *A*) provide verified (Lee et al., 1999) measures of relative network density, $\bar{\rho}$, as well as λ_1 and λ_2 along a micropipette-aspirated projection of network (Discher and Mohandas, 1996). Axisymmetry is assumed with the *2*-direction taken as the circumferential direction and the *1*-direction along the meridian:

$$\lambda_1 = 1/(\bar{\rho}\lambda_2) \tag{4a}$$

$$\lambda_2(z') = \frac{r(z')}{R_p}\left\{\left(\frac{R_{so}}{R_p}\right)^2 - \left[\left(\frac{R_{so}}{R_p}\right) - \left(\frac{l}{R_{so}}\right)_{tip}\int^{z'}\bar{\rho}\,dz'\right]^2\right\}^{-1/2} \tag{4b}$$

The upper limit on the integral, z', is the axial distance from the tip of the projection. The radial distance from the axis of symmetry is given, for $z' \geq R_p$, by $r(z') = R_p$; and the reference sphere of the same area as the deformed cell has a radius given by R_{so}. Generically, the "mean" stretch ratio λ_1 in the direction of the micropipette axis is ~2 or more over much of a projection's length ($L/R_p \gtrsim 4$; $z'/R_p \gtrsim 1$). In contrast, λ_2 in the circumferential direction is typically ~0.5 or less. Such kinematic results, with minor qualification, were directly confirmed by fluorescence patterned photobleaching (Lee et al., 1999). Knowing λ_1 and λ_2 pointwise allows subsequent estimation of filament reorientation using Eq. 3a. Fig. 4 *A* illustrates a distribution of actin that is typical of earlier results (Discher et al., 1994, 1996) and which readily yields, via Eqs. 3 and 4, a pointwise

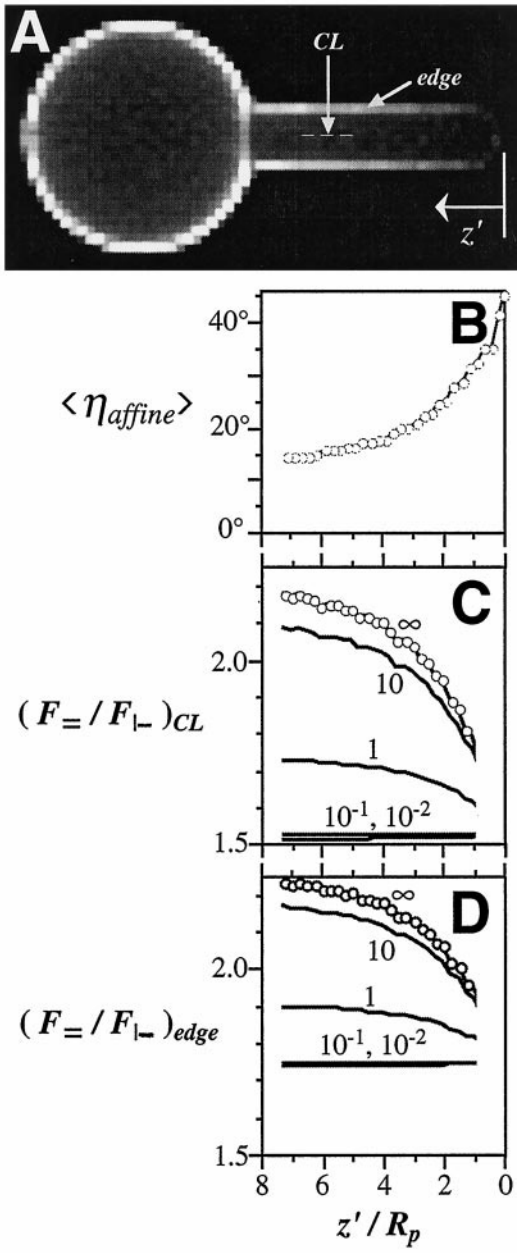

FIGURE 4 Membrane actin distribution in a micropipette aspirated cell together with affine model predictions for protofilament rotations on the projection. (*A*) Monte Carlo simulated network as a plane-projected image. Such simulated distributions are shown to be in extremely good agreement with experiment (Discher et al., 1998) and lead to very reliable determinations of network stretch ratio distributions, λ_1 and λ_2 (Lee et al., 1999). (*B*) Mean filament angle with respect to the z direction according to the affine model of Eq. 3a. (*C* and *D*) Predicted polarization ratios along either the centerline or the edge of the aspirated projection, as estimated using Eqs.1 and 2 together with the thermal-affine model. In this average affine angle defines the angle of minimum energy and other filament orientations contribute to the signal according to their Boltzmann weight (Eq. 6). Each curve corresponds to a rotational elastic constant in units of k_BT that varies from large (∞) to small.

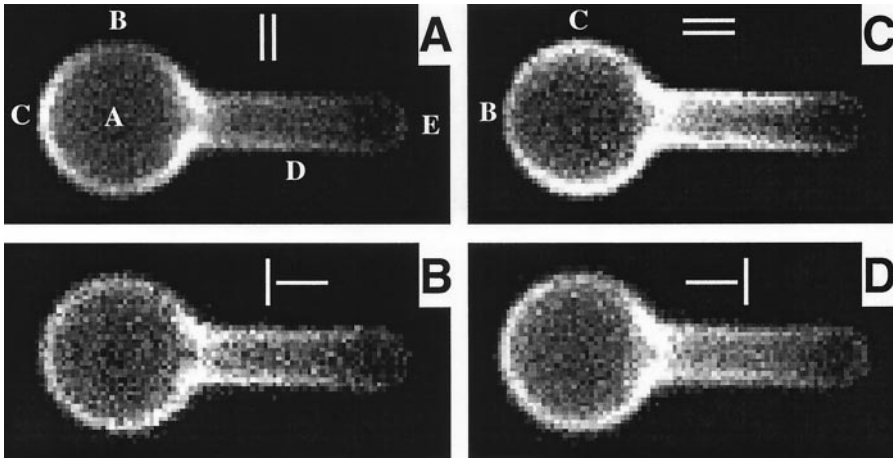

FIGURE 5 Polarization images of a single, micropipette-aspirated, actin-labeled cell with a relative projection length of $L/Rp = 6.4$, where the micropipette radius is $R_p = 0.7$ μm. The locations of membrane points B and C on all four images are determined by the excitation polarizer orientation, which is perpendicular to the micropipette in *A* and *B* and parallel to the micropipette in *C* and *D*.

computation of the average reorientation angle $\langle \eta_{\text{affine}} \rangle$ along the projection (Fig. 4 *B*). Additional calculations with a model projection half the size of the one analyzed here yield overlapping results, suggesting a relatively weak dependence of polarization ratios on aspirated projection length, L/R_p, although ratios can depend strongly on position z' along a given projection.

FPM image predictions

By employing Eqs. 1 and 2 for fluorescence polarization ratios, distributions for η such as those in Fig. 3 *B* can be readily converted to spatial distributions of fluorescence polarization ratios. Along an aspirated projection, this is very easily done at the centerline, where η corresponds to an angle in a tangent plane that is parallel to the X_2-X_3 plane. Equation 2a for $(\eta_{23} I_{\parallel} / \eta_{23} I_{\perp})$ then applies to any single filament at a point z' along the centerline, and one must simply determine the average fluorescence signal emanating from the collection of protofilaments at z'. The cumulated ratio denoted by $\langle F_{=}/F_{\dashv} \rangle_{\text{CL}}$ along the centerline corresponds to the excitation polarizer being parallel to the micropipette, which is always taken to be horizontal; whereas the ratio denoted by $\langle F_{\parallel}/F_{\dashv} \rangle_{\text{CL}}$ corresponds to the excitation polarizer being perpendicular to the micropipette. To illustrate the computations, η_i is defined as the angle with respect to the micropipette axis (z axis) that is made by the *i*th protofilament (of N protofilaments at z'):

$$\langle F_{=}/F_{\dashv} \rangle_{\text{CL}} = \frac{1}{N} \sum_{i=1}^{N} P(\eta_i)(1.0 + 1.4 \cos^4 \eta_i) \qquad (5)$$

Because distributions for η_{affine} vary pointwise with the kinematic quantities $\bar{\rho}$, λ_1, and λ_2, such polarization ratios should generally be z'-dependent along the centerline as well as along the outer edge of the cylindrical projection. Calculated profiles for $\langle F_{=}/F_{\dashv} \rangle_{\text{CL}}$ and $\langle F_{=}/F_{\dashv} \rangle_{\text{edge}}$ under the assumed affine deformation are shown, respectively, in Fig. 4, *C* and *D*, as the curves composed of circular points. Definitive gradients in fluorescence polarization ratios emerge, and the intensity ratio magnitudes are generally within reliable detection limits of FPM, as evidenced by Fig. 2.

Thermal fluctuations around affine means

The above affine reorientations do not include azimuthal fluctuations. For initial purposes, a "bounded" Gaussian is assumed about the affine angle $\eta_{\text{i-affine}}$ of the *i*th protofilament. To capture this, each protofilament in a local ensemble is assumed to spin through a maximum difference angle ($\pm\ \delta\eta =)\ -180°$ to $+180°$ relative to $\eta_{\text{i-affine}}$. The width of the (unbounded) distribution is set by the elastic constraints imposed by the spectrin chains; i.e.,

$$P(\delta\eta_i) \sim \exp(-k_{\text{rot}} \delta\eta_i^2 / k_B T) \qquad (6)$$

With this used in calculations typified by Eq. 5, the FPM signal becomes a weighted average of the signal resulting from the angular states distributed about $\eta_{\text{i-affine}}$. As an example, suppose for the *i*th filament that $\eta_{\text{i-affine}} = 15°$ with respect to the z axis of extension; then $\eta_i = 15° + \delta\eta_i$ and $\eta_i = 15° - \delta\eta_i$ will both occur as thermal fluctuations of equal probability, $P(\delta\eta_i)$, but will make very different contributions to the signal. It is not surprising that the average signal does not precisely correspond to the signal of the average state. In general, the *i*th filament's contribution to the FPM signal, for $\eta_i < 45°$, is lower than the signal of the average; whereas the opposite is true for $\eta_i > 45°$. The difference in fact grows with increased fluctuations (i.e., greater variance). However, as a consequence of the large number of reoriented protofilaments at small angles ($\eta_i < 45°$), there is a strong tendency for reduced polarization ratio signals due to thermal fluctuations when compared

with the rigid limit of pure affine response illustrated by the aforementioned curve of circular points $T = 0$ ($k_{rot}/k_BT = \infty$). Computed results for finite (k_{rot}/k_BT) varying from 10 down to 0.01 are shown in Fig. 4, *C* and *D*. Clearly, with smaller elastic constants, the gradients in polarization intensity ratios diminish along the aspirated projection. This feature is among the essential diagnostics for distinguishing between two possible cases: $T = 0$ affine behavior and a thermally fluctuating, softly intercoupled elastic network. In sum, thermal fluctuations tend to wash out any tendency for filaments to reorient in deformation. What is not clear, however, is whether local deformation of the network modulates the effective elasticity via such conceivable mechanisms as steric crowding and nonlinear chain elasticity. This is among the principal issues addressed by FPM of micropipette-aspirated cell ghosts.

RESULTS

Actin protofilament orientation in a resealed ghost pulled into a micropipette

To assess a possible reorientation of actin protofilaments as a cell membrane is controllably deformed, a series of polarization images was collected of individual erythrocyte ghosts pulled into a micropipette after labeling with rhodamine phalloidin. A representative set of four images taken with either parallel or crossed polarizers is shown in Fig. 5. Several features are particularly distinctive in the two images with else both polarizers perpendicular (Fig. 5 *A*) or both polarizers parallel (Fig. 5 *C*) to the micropipette axis. First, along the spherical contour of membrane outside the micropipette, the points having the highest and lowest intensities and labeled as points C and B, respectively, are transposed between images. Second, a more pronounced decrease in fluorescence intensity along the cylindrical projection toward the tip is observed through polarizers that are both parallel (Fig. 5 *C*) as opposed to perpendicular (Fig. 5 *A*) to the micropipette axis. In contrast, when the polarizers are oriented perpendicular (Fig. 5 *A*) to the micropipette axis, a higher intensity is discernible at the very tip of the projection's cap.

A line profile along the micropipette's centerline (Fig. 6) illustrates the three central features just identified. Quantitatively different profiles are obtained with polarizers either both parallel or both perpendicular to the micropipette. Each profile's minimum intensity to the left of the micropipette entrance near $z = 0$ corresponds to the center of the spherical portion of the cell ghost (designated point A), and these minima appear to be independent of polarizer orientation. This is consistent with expectations that actin should have a random azimuthal orientation on the outer spherical contour.

When both polarizers are oriented perpendicular to the micropipette (i.e., ‖), the resulting intensity profile often has

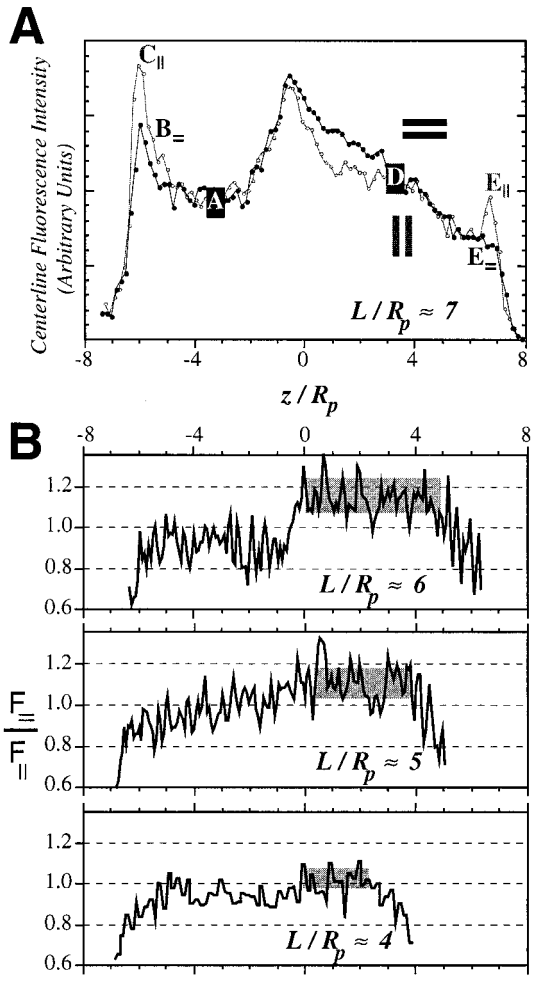

FIGURE 6 Centerline intensity profiles (*A*) or intensity ratios (*B*). Excitation and emission polarizers are parallel to each other, and both are either parallel (═) or perpendicular (‖) to the micropipette axis. In *A*, R_p = 0.76 μm. The labeled points A and E represent, respectively, the center of the outer sphere or the tip of the aspirated projection. In *B*, a weak trend emerges for protofilament alignment in the network-stretched *z* direction. These regions are highlighted in gray; the projection's midpoint D is generally seen to be a good characteristic.

a concave-up curvature along the projection, decreasing with *z* more abruptly near the micropipette entrance than near the tip or cap of the cell. In contrast, when both polarizers are parallel to the micropipette axis (i.e., ═), the profile has an almost concave-down appearance with an equal or steeper slope toward the cap of the projection. Qualitatively, the tip of the aspirated projection in Fig. 6 (designated point E) gives an immediate impression that the filaments lie tangent to the bilayer, conforming to the hemispherical cap.

Key intensity ratios obtained from the spherical segment of membrane outside the micropipette are compiled in Fig. 7 *A* and are found to be largely identical to ratios obtained with osmotically sphered ghosts (Table 1 in Picart and

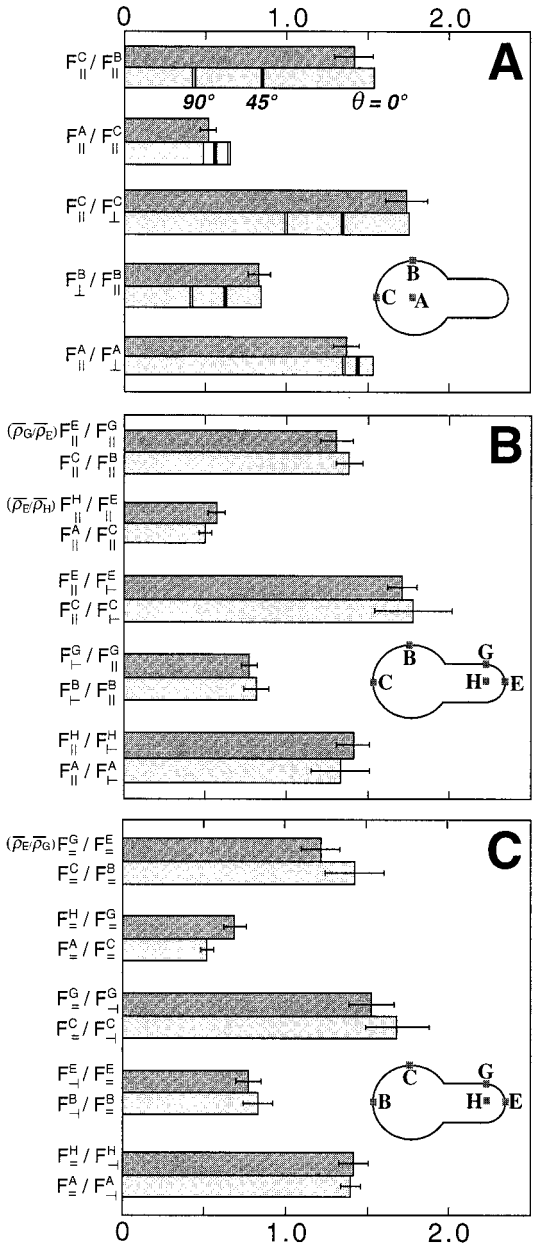

FIGURE 7 FPM intensity ratios for actin-labeled ghosts aspirated into micropipettes (seven ghosts; averages ± SD). (*A*) Intensity ratios for points on the outer spherical segment of membrane, as sketched in the inset. Measured ratios are compared to filament ensemble model estimates (Picart and Discher, 1999), where the protofilaments are all either tangent ($\theta = 0°$, *single line*), inclined at 45° (*solid line*), or perpendicular ($\theta = 90°$, *double line*) to the membrane. Experimental averages pool together such ratios as $F^{C}_{=}/F^{B}_{=}$ and $F^{C}_{\parallel}/F^{B}_{\parallel}$, because no significant differences were found between such symmetrical pairs. (*B*) Characteristic ratios at the hemisperical cap (*dark gray*) of the aspirated projection when the excitation polarizer is oriented perpendicular to the pipette axis (*dark gray*). To isolate the relative polarization differences between the point E and points G and H, a relative network density difference of ~15% (Discher and Mohandas, 1996) is suitably factored out of the measured intensity ratios. Cap ratios are paired with homologous ratios from the outer spherical segment (*light gray*). (*C*) Similar to *B*, except that the excitation polarizer is oriented parallel to the micropipette axis. Note that the points B and C are transposed, with the point C always being identified as the point at which the excitation polarizer is tangent to the outer spherical segment.

Discher, 1999). Indeed, the filament ensemble model elaborated in detail by Picart and Discher (1999) again fits the data well. Briefly, the single-filament results illustrated in Fig. 2 and summarized in Eq. 2 were integrated into a protofilament orientation model where a random azimuthal angle, η, about the membrane normal was averaged over $[0, \pi/2]$, and the best-fit angle, θ, with respect to the bilayer was deduced. When we compared the model to experimental results, $\theta \lesssim 20°$ appeared to yield an excellent fit of four of the five key ratios, with the exceptional ratio ($F^{A}_{\parallel}/F^{A}_{\perp}$) standing out as the one with the smallest theoretical dependence on θ. It thus seems clear that the spherical portion of the micropipette-aspirated cell is relatively unperturbed referenced to a red cell ghost that is either osmotically swollen or discocytic, as elaborated by Picart and Discher (1999).

Noting that the relatively unstrained outer spherical contour and the network-dilated, hemispherically capped tip of the projection have a common shape, we formed polarization ratios from intensities at points on the cap designated E, G, and H in Fig. 7, *B* and *C*. These are compared, in context, to homologous ratios formed from points A, B, and C. For instance, ratios involving the points G and E would be homologous to those involving the points B and C, depending on the polarizer orientation. One slight complicating factor must be included, however: actin densities differ between the point E and the points G and H, whereas actin density is nominally the same at points A, B, and C. Density-corrected ratios remove this difference by inclusion of a numerical factor measured from images obtained in the absence of any polarizers and well approximated (due to near-linear density gradients) as 0.85 or its inverse. By including this relative density correction, the average ratio involving intensities at the points G and E, e.g., $(\bar{\rho}_E/\bar{\rho}_G)$ $F^{E}_{\parallel}/F^{G}_{\parallel}$, is within a few percent of the homologous average ratio obtained from the outer sphere, i.e., $F^{C}_{\parallel}/F^{B}_{\parallel}$. In this particular set of homologous pairs, a maximum difference of 17% for any one cell ghost was found between the ratios $F^{G}_{=}/F^{E}_{=}$ and $F^{C}_{\parallel}/F^{B}_{\parallel}$. Partial explanation may lie in the fact that the points B, G, and H are difficult to locate because of their low intensities. Despite this, all other ratios involving the points G and H were within 7% of homologous ratios outside the pipette.

Because membrane curvature was shown to have only a weak effect on ratios involving A, B, and C (Picart and Discher, 1999), the finding of comparable results at E, G, and H indicates that the tangent angle orientation of actin protofilaments is essentially the same on the unstrained outer sphere and the hemisperical cap. This is confirmed by the ratios, which the tangent orientation model predicts to be 1.74 for $F^{C}_{\parallel}/F^{C}_{\vdash}$ and 0.48 for $F^{A}_{\parallel}/F^{C}_{\parallel}$, respectively. We therefore conclude that the protofilaments are essentially tangent to the membrane, despite the considerable network strain—and presumably forces on actin—at the cap.

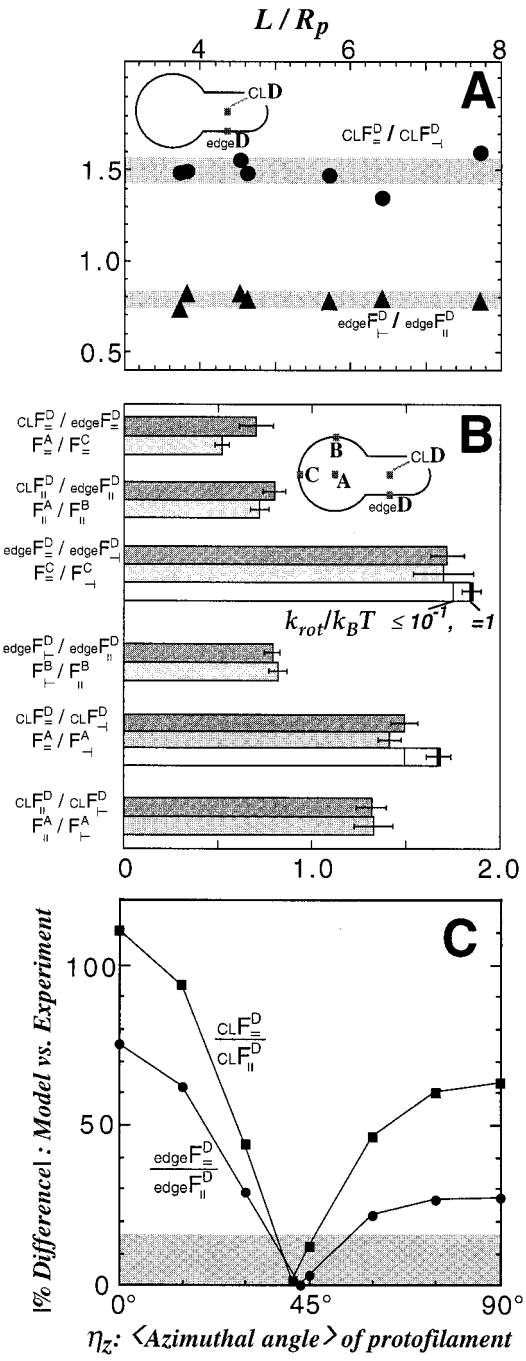

FIGURE 8 FPM intensity ratios for the midpoint of the aspirated projection of actin-labeled ghosts (seven ghosts). (*A*) Two ratios were obtained from intensities at either the center line, ${}_{CL}F^{D}_{\parallel}/{}_{CL}F^{D}_{\vdash}$, or the projection's edge, ${}_{edge}F^{D}_{\vdash}/{}_{edge}F^{D}_{\parallel}$. These ratios appear to be independent of the aspirated projection length, L, scaled by the micropipette radius ($R_p = 0.5$–0.9 μm). (*B*) Average intensity ratios at the midpoint of the aspirated projection, either at the centerline (CL) or at the edge. The midpoint ratios are paired with homologous ratios obtained from the outer spherical segment of membrane. Model calculations for the two ratios shown in Fig. 4, *C* and *D*, along the entire projection are also shown for comparison. (*C*) Relative difference between experiment and filament ensemble model estimates for two midpoint polarization ratios. The average azimuthal angle, η, is defined with respect to the micropipette axis, i.e., $\eta \rightarrow 0°$ corresponds to all filaments aligning with the micropipette axis. For the model estimates, it is assumed that $\theta = 0°$. The minimum difference between model and experiment occurs in the neighborhood of $\eta = 45°$; the shaded zone indicates the range of error (~17%) typical of FPM measurements (Axelrod, 1979; Picart and Discher, 1999). Very similar results are obtained for ratios involving crossed polarizers. The bars capped by numbers correspond to the most relevant computations shown in Fig. 4, *C* and *D*.

FPM of F-actin at the midpoint D along the aspirated projection.

To assess the orientation of filaments along the projection, several ratios involving the center line and edge intensities at the projection midpoint D were calculated. It was first found that the key ratios $({}_{CL}F^{D}_{=}/{}_{CL}F^{D}_{\vdash})$ and $({}_{edge}F^{D}_{\parallel}/{}_{edge}F^{D}_{\vdash})^{-1}$ at point D exhibited no dependence on the projection length (Fig. 8 *A*). It was next found that ratios involving the point D are practically indistinguishable from like ratios at both the point A and, very importantly, the point H. That is, there appears to be no significant gradient in intensity ratio along the aspirated projection. Six ratios involving point D are tabulated in Fig. 8 *B*, together with their analogous ratios from the outer sphere. Comparable ratios between the projection and the outer sphere generally were within a few percent; the worst case was $({}_{CL}F^{D}_{=}/{}_{edge}F^{D}_{=})$ and was found to be just outside the standard deviation of its homologous ratio. Physical explanation for this will be given in clarifying results below for band 3. All of the ratios therefore provide the strong impression that the cumulated orientation of the actin protofilaments on the highly stretched part of the aspirated network is very close if not identical to that of the filaments on the outer, unstrained contour of membrane.

Hypothesized redistributions for $P(\eta_{affine})$ are strongly skewed at zero temperature as shown in Fig. 3 *B* and indicate the emergence of a much smaller and dominant $\langle\eta_{affine}\rangle$, as illustrated in Fig. 4 *B*. Assuming that the protofilaments remain tangent to the lipid bilayer, Eq. 2 together with the symmetry of crossed polarizers and $\{=: y = X_2, z = X_3\}$, $\{\|: y = X_3, z = X_2\}$ imply that

$$(I_{=}/I_{\|}) = \frac{(1.0 + 0.35\,N_x^4 + 1.4\,N_z^4)}{(1.0 + 0.35\,N_x^4 + 1.4\,N_y^4)} \tag{7a}$$

which allows a very simple determination of pipette-parallel over pipette-perpendicular intensity ratios, provided the average azimuthal angle $\eta_z = \langle\eta_{affine}\rangle$ is used without any further averaging. Thus, if we ignore small curvatures, then at the point D_{CL}, where bilayer-tangent protofilaments have no component along the optical axis (i.e., $N_x^2 \approx 0$), and at the point D_{edge}, where $N_y^2 \approx 0$, we arrive at

$$(F_{=}/F_{\|})_{CL} \approx (1.0 + 1.4\,N_z^4)/(1.0 + 1.4\,N_y^4) \tag{7b}$$

$$(F_{=}/F_{\|})_{edge} \approx (1.0 + 0.35\,N_x^4 + 1.4\,N_z^4)/(1.0 + 0.35\,N_x^4) \tag{7c}$$

Given experimental determinations of $(F_{=}/F_{\parallel})_{\mathrm{DCL}} \approx 1.14 \pm 0.07$ and $(F_{=}/F_{\parallel})_{\mathrm{Dedge}} \approx 1.37 \pm 0.07$, and given that, in each tangent plane, there is only the one angle that enters the analysis (because $\mathbf{N} = 1$), we can solve Eqs. 7b and 7c for η_z (i.e., N_z) These are found to be $\sim 41° \pm 2°$ at the centerline and $\sim 43° \pm 3°$ at the edge. The significance of these determinations is emphasized by plotting the relative difference between experiment and model estimates for $(F_{=}/F_{\parallel})_{\mathrm{CL\ D}}$ and $(F_{=}/F_{\parallel})_{\mathrm{edge\ D}}$, as shown in Fig. 8 *C*. Allowing for a generic error of ~17% between experiment and models (Picart and Discher, 1999), mean angles ranging from $45° \pm 10°$ are not inconsistent with the data; clearly, however, mean angles between 15° and 30° as predicted by the zero-temperature affine model (Fig. 4 *B*) are not consistent with the data. If one thus assumes that there is a well-defined reorientation of the protofilaments in network deformation and then determines the average angle that is most consistent with experiment, the resulting average of ~45° is indistinguishable from the 45° average of an essentially flat and random distribution, as shown in Fig. 3 *B* (*left*).

Comparison with FPM of band 3 in a resealed ghost pulled into a micropipette

For comparison to the FPM results with actin, the transmembrane protein band 3 was labeled with EMA, and ghosts were imaged while being held in the micropipette. At least on undeformed cells, about one-third to two-thirds of band 3 molecules are specifically linked to network spectrin via ankyrin (Tsuji et al., 1988). These still rotate, but with a time constant that is long compared with typical fluorescence lifetimes; the remaining band 3 is more freely diffusing, although steric interactions with the subjacent network appear to decrease band 3 translational diffusivity. Deformation of the underlying network in micropipette aspiration does not appear to greatly impede translational motions, at least, of band 3 (Discher and Mohandas, 1996). The results of Fig. 9 suggest that band 3 on the aspirated projection differs insignificantly in orientation compared to band 3 on the outer unstrained contour of membrane. Fig. 9 *A* shows first, however, a good comparison between our results and those reported in a confocal FPM study by Blackman et al. (1996) of EMA-labeled ghosts. The only intensity ratio that differs significantly is that associated with point B. However, the intensities at this point can be difficult to quantitate accurately, because the edge signal is lowest at point B. Moreover, FPM by confocal microscopy would tend to be more signal limited. Regardless, the method-consistent comparisons in Fig. 9 *B* between intensity ratios at the network deformed point D and the outer points, A, B, and C, indicate no strong reorientation effect in micropipette aspiration. The greatest difference appears, as with actin imaging, in the centerline-to-edge intensity ratio, ${}_{\mathrm{CL}}F^{\mathrm{D}}_{=}/{}_{\mathrm{edge}}F^{\mathrm{D}}_{=}$, which is, in comparing means, 27% more than the homologous ratio $F^{\mathrm{A}}_{=}/F^{\mathrm{C}}_{=}$. The same comparison for actin protofilaments (Fig. 8 *B*) also showed the greatest difference in these FPM ratios, with the mean for the ratio at point D being greater by 26%. As recognized by Axelrod (1979), however, point A is out of focus, and a corrective increase in the A-to-C ratio should be made in comparison with any in-focus values. Because the centerline and edge points at D inside the ~1.5-μm-diameter micropipettes are both essentially within the plane of focus of the microscope objective used (e.g., Hiraoka et al., 1987), Axelrod's estimated decrease of ~25% of the in-focus value (theoretical or not) brings these CL-to-edge ratios, for both band 3 and actin, into excellent agreement with the homologous A-to-C ratios.

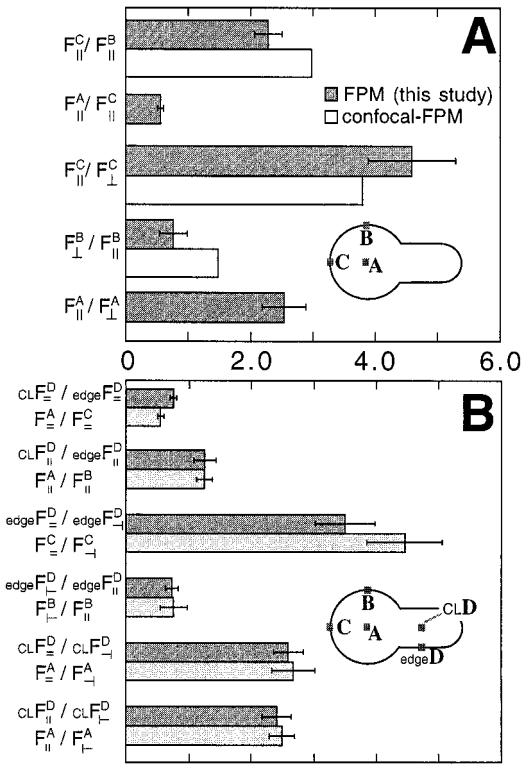

FIGURE 9 Polarization ratios for EMA-band 3-labeled ghosts aspirated into micropipettes. (*A*) Intensity ratios for points on the outer spherical segment of membrane. Ratios were averaged for like pairs of polarizers (six ghosts; averages ± SD). Confocal FPM results of Blackman et al. (1996) (as estimated from Blackman's figure 5) are shown for comparison. (*B*) Intensity ratios at the midpoint of the aspirated projection, either at the centerline (CL) or at the edge, are plotted adjacent to homologous ratios from the outer spherical segment of membrane.

Finally, because the ratio $({}_{\mathrm{edge}}F^{\mathrm{D}}_{=}/{}_{\mathrm{edge}}F^{\mathrm{D}}_{\vdash})/({}_{\mathrm{edge}}F^{\mathrm{D}}_{\parallel}/F^{\mathrm{D}}_{\vdash}) = 1.89 \pm 0.31$ is within 17% of the homologous ratio $F^{\mathrm{C}}_{\parallel}/F^{\mathrm{B}}_{\parallel} = 2.28 \pm 0.22$, a random azimuthal orientation for band 3 along the projection is once again indicated.

DISCUSSION

FPM applied to rhodamine-phalloidin-labeled actin protofilaments in micropipette aspiration indicates that protofila-

ments everywhere tend to remain tangent to the bilayer. This tangent orientation persists despite 1) spectrin-exerted stresses at curved contours such as the hemispherical cap of the projection, where the network is dilated; 2) large anisotropic strains induced along the aspirated projection; and 3) high network compression near the micropipette entrance. This proves consistent with a strong multipoint interaction between a protofilament and its associated protein 4.1 glycophorin C linkages (Fig. 1 *B*). Such a multipoint constraint was previously concluded from FPM of actin in discocytic and sphered red cell ghosts; the present study indicates further that the relevant interactions are not extremely labile under network stress.

Surprisingly, however, actin protofilaments that appear in undeformed membranes to have random azimuthal angles continue to exhibit random azimuthal orientations in very large deformation of the spectrin network. This contrasts with both the zero-temperature, affine deformation hypothesis for filament reorientation (in the Theoretical Preliminaries) and full, finite-temperature simulations of coarse-grained spectrin network triangulations (Fig. 10); both approaches lead one to expect that filaments reorient in the direction of strongest spectrin stretch, which is parallel to the micropipette axis. Moreover, predicted gradients in polarization ratios illustrated in Fig. 4, *C* and *D*, as well as Fig. 10 *C*, would certainly be within the range of detectability by FPM for large values of the rotational elastic constant (i.e., $k_{rot}/k_BT \sim 5$ to ∞). In experiments, these gradients would lead, in particular, to measurable differences in polarization ratios along the centerline at the points D and H, as well as at least some dependence on aspirated projection length, i.e., network deformation. Neither actin protofilaments nor band 3, however, exhibits any difference in FPM ratios at the points D and H, even when compared with the FPM ratios from the relatively undeformed point A, where a random azimuthal orientation is fully consistent with previous conclusions (Picart and Discher, 1999).

Persistent randomness could have at least two origins. First, thermal fluctuations opposed by an effective torsional spring constant, k_{rot}, for the network, as shown in Fig. 4, *C* and *D*, would tend to wash out any reorientation. A second possibility is that the deformation is in no simple way affine; the presumption that actin rotates while spectrin rotates and extends might seem a logical intermixing of the continuum view of the network (Evans and Skalak, 1980) with a discrete assembly of cytoskeletal proteins. However, Fig. 11 clearly illustrates how protofilaments could end up counter-rotating in network extension rather than skewing into the direction of maximum extension. The effective elastic coupling constant between network stretch and protofilament orientation could thus be weak because of quenched spin-glass-like frustration (e.g., Franzese, 2000). For a continuous medium, as alluded to in the Introduction, the coupling constant between rotation of a material filament and the external deformation would ordinarily be on the same order as k_{rot} and be related to the shear modulus of the media. From linear elasticity (e.g., Landau and Lifshitz, 1986), it can be shown that

$$k_{rot} = 2\pi\alpha\mu L^2 \quad (8)$$

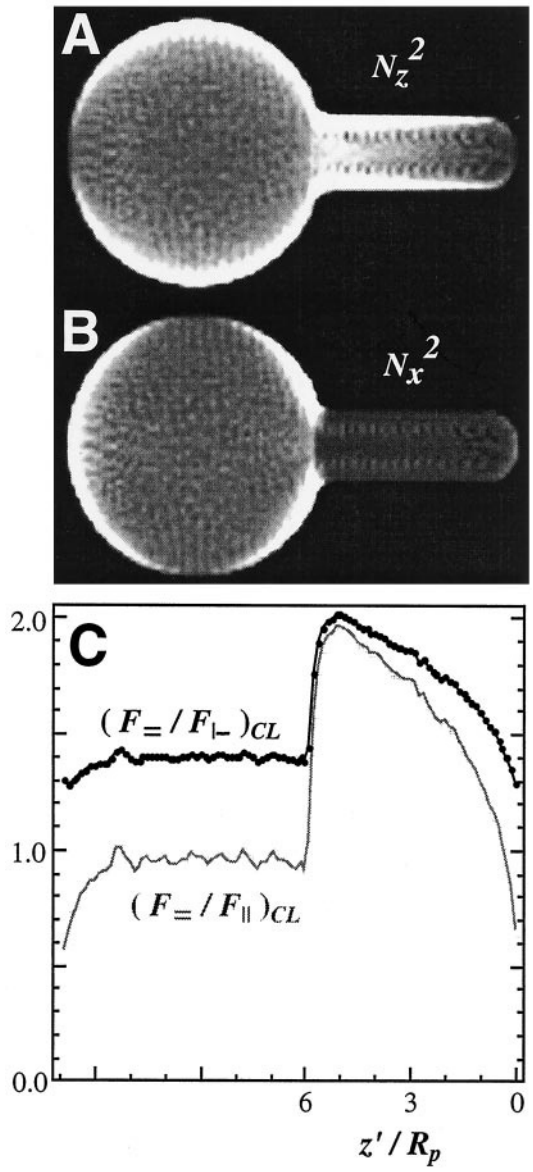

FIGURE 10 Spectrin network simulations exhibiting strong reorientation of tethers in deformation. (*A* and *B*) Images are projections of spectrin tether components into the X_2-X_3 plane as calculated from statistical mechanical simulation of coarse-grained triangulated networks (per Discher et al., 1998). Pixel size approximates the resolution limit of the microscope. (*C*) Intensity ratio profiles were calculated along the centerline, using either Eq. 2 or Eq. 7 in the text. The top curve, in the interval $1 \leq z'/R_p \leq 6$, should be compared with the finite-temperature affine model of Fig. 4 *C*; the comparison suggests that the triangulated network corresponds to a structure with $(k_{rot}/k_BT) \sim 5$ and 10. This is unlike experiments illustrated by Figs. 5 and 6 and indicates, for actin, a more complex but disordered nanoresponse in the network.

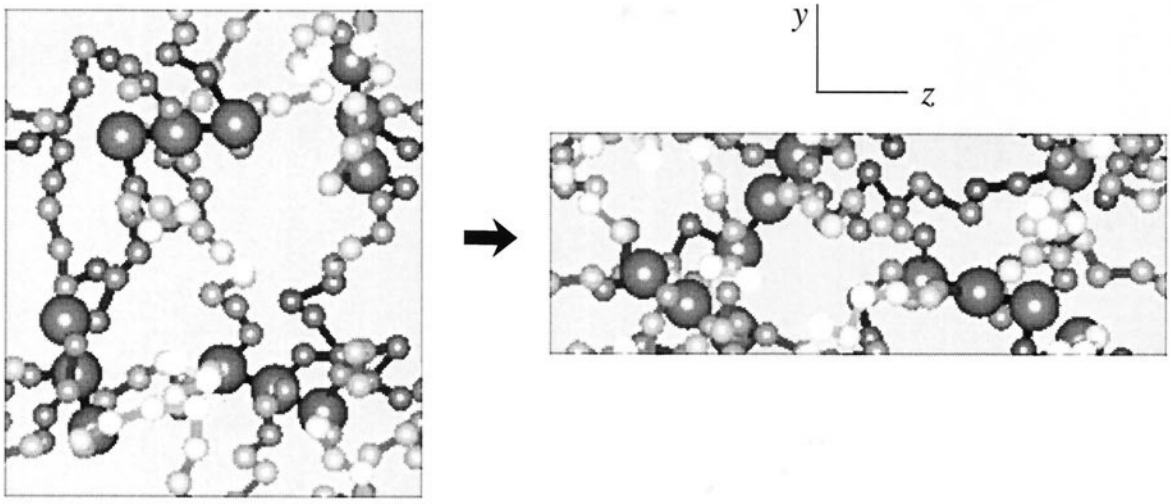

FIGURE 11 Monte Carlo simulations of four short and stiff actin protofilaments interconnected by flexible, multikinked spectrin chains. At the vertex of each spectrin kink is a spherical "domain" half the diameter of an actin particle. (*Left*) An unstressed state, where chain tension balances against excluded volume. (*Right*) Tension is applied to the network in the extended direction, while compression is applied in the contracted direction to achieve an average state much like that in Fig. 1 *A*.

where α is a constant that characterizes filament coupling to network shear, μ is the two-dimensional network shear modulus, and L is the filament length. In the tight coupling limit, $\alpha = 1$. For weaker coupling of material filament rotations to shear strains in the embedding network, $\alpha < 1$. Given a red cell shear modulus of $\mu \sim 0.005$ pN/nm (Evans and Skalak, 1980) and an actin protofilament length $L \sim 35$ nm, $k_{rot}/k_BT \sim 10\alpha$. Because all of the experimental results (Figs. 7 and 8) suggest that the most realistic model curves in Fig. 4, *C* and *D*, correspond to $k_{rot}/k_BT \leq 1$, we conclude that $\alpha \leq 0.1$. The implied loose coupling is not uncommon to other soft, biophysical systems: mechanical extension of myotubes in rigor will generate a predictable shear angle of the myosin lever arm, but only a fraction of the expected rotation is measured in very thorough fluorescence polarization experiments (Y. Goldman, personal communication).

The snapshots of Fig. 11 are taken from Monte Carlo simulations in which each of four short actin protofilaments is modeled as a stiff trimer of beads cross-linked together by longer, more flexible spectrin chains. The isothermal-isobaric ensemble is essentially the same as that described by Boey et al. (1998) (further details are given in the Appendix). Importantly, the spectrin-actin interconnections are fixed at the outset with exactly two spectrin chains per actin bead, summing to six spectrin chains per model protofilament. The connectivity is otherwise random. Any initial bead overlaps are annealed away by simulating with soft repulsive interactions until no bead overlaps occur; hard-core sterics are implemented from that point on, and statistics are developed for several different initial network connectivities. Using the above algorithm for initialization, it is found that polarization imaging of the model protofilaments, by use of Eq. 2, leads to a signal that appears either random or else very close to random:

$$F_{=}/F_{|-} = 1.56 \pm 0.31 \text{ (unstressed)}$$

$$F_{=}/F_{|-} = 1.69 \pm 0.39 \text{ (stressed)}$$

Most importantly, the present set of simulations (Table 1) shows that, more than half the time, stressing the network leads to a counter-rotation away from the average initial angle rather than an alignment in the spectrin-extended direction. Thermal, rotational fluctuations are also tabulated. With Eqs. 6 and 8 indicating $\langle \delta\eta^2 \rangle \approx 7°\alpha^{-1}$ and Table 1 listing $\langle \delta\eta^2 \rangle \approx 44°$ (unstressed), 35° (stressed), thermal fluctuations alone indicate $\alpha \sim 0.2$.

CONCLUSIONS

The "vertical" linkage of actin to the overlying membrane is clearly strong. It is able to resist detachment forces that are normal to the membrane as should arise, in particular, at the tip of a microprojection where large network dilation is found. Such results may be relevant and the methods useful to echinocytic red cells having many "spontaneously" formed surface microprojections. However, in-plane elastic coupling between network shear and protofilament rotation is weak. Both thermal fluctuations and nanoscale connectivity have a strong disordering influence, even in highly extended networks.

TABLE 1 Subset of ensemble-averaged simulation results for the orientations and reorientations of trimer filaments in spectrin-actin connected configurations that are either unstressed or stressed in the *z* direction (Avg. ± SD)

Spectrin-actin connectivity	Filament 1		Filament 2		Filament 3		Filament 4	
	η_z (°)	$F_=/F_\vdash$	η_z (°)	$F_=/F_\vdash$	η_z (°)	$F_=/F_\vdash$	η_z (°)	$F_=/F_\vdash$
No. 1								
Unstressed	2 ± 62	1.29 ± 0.42	−3 ± 15	2.22 ± 0.21	8 ± 69	1.16 ± 0.30	−11 ± 22	2.05 ± 0.35
Stressed	−8 ± 59	1.30 ± 0.41	−6 ± 23	2.04 ± 0.33	11 ± 65	1.20 ± 0.33	−9 ± 29	1.91 ± 0.40
No. 2								
Unstressed	−26 ± 15	1.86 ± 0.36	40 ± 45	1.27 ± 0.37	6 ± 16	2.21 ± 0.23	−34 ± 40	1.46 ± 0.46
Stressed	−22 ± 28	1.78 ± 0.45	−15 ± 48	1.58 ± 0.53	35 ± 24	1.65 ± 0.47	8 ± 64	1.23 ± 0.39
No. 3								
Unstressed	2 ± 32	1.86 ± 0.42	35 ± 31	1.55 ± 0.48	26 ± 28	1.73 ± 0.46	12 ± 29	1.87 ± 0.41
Stressed	11 ± 36	1.85 ± 0.49	26 ± 63	1.16 ± 0.31	32 ± 43	1.47 ± 0.50	26 ± 46	1.50 ± 0.49

APPENDIX

Although a fuller account of the spectrin-actin network simulations will be given elsewhere, we simply note here that the phase space statistics in Table 1 are obtained from convergent simulations containing at least 3×10^5 Monte Carlo steps. The spectrin chains consist of 10 beads of diameter d tethered together; the actin beads are twice the diameter of spectrin beads, and stiff, harmonic potentials make the model protofilaments rigid in both bending and stretching. Actin is confined to the $z = 0$ plane, while spectrin beads fluctuate above this plane. When the two-dimensional pressure is exactly zero, the periodic box containing the network fluctuates freely and independently in the y and z directions. When tensed by $5k_BT/d^2$ in the z direction and compressed by $-5k_BT/d^2$ in the y direction, the network elongates, with average stretching given by $\langle L_z\rangle/\langle L_z\rangle_o = 1.94 \pm 0.10$ and $\langle L_y\rangle/\langle L_y\rangle_o = 0.52 \pm 0.05$.

The authors thank Prof. Henry Shuman, Prof. Yale Goldman, Dr. Vladimir Zhukarev, and the Sanger Laboratory for the valued help and early discussions concerning fluorescence polarization.

This work was supported in part by the Whitaker Foundation (DED), the National Institutes of Health (R01-HL62352-01 to DED), and by the Fondation pour la Recherche Medicale (CP).

REFERENCES

Alloisio, N., N. Dalla Venezia, A. Rana, K. Andrabi, P. Texier, F. Gilsanz, J. P. Cartron, J. Delaunay, and A. H. Chishti. 1993. Evidence that red blood cell protein p55 may participate in the skeleton-membrane linkage that involves protein 4.1 and glycophorin C. *Blood.* 82:1323–1327.

Axelrod, D. 1979. Carbocyanine dye orientation in red cell membrane studied by microscopic fluorescence polarization. *Biophys. J.* 26: 557–574.

Bennett, V., and P. J. Stenbuck. 1979. The membrane attachment protein for spectrin is associated with band 3 in human erythrocyte membranes. *Nature.* 280:468–473.

Blackman, S. M., C. E. Cobb, A. H. Beth, and D. W. Piston. 1996. The orientation of eosin-5-maleimide on human erythrocyte band 3 measured by fluorescence polarization microscopy. *Biophys. J.* 71:194–208.

Boey, S. K., D. H. Boal, and D. E. Discher. 1998. Simulations of the erythrocyte cytoskeleton at large deformation I: microscopic models. *Biophys. J.* 75:1573–1583.

Byers, T. J., and D. Branton. 1985. Visualization of the protein associations in the erythrocyte membrane skeleton. *Proc. Natl. Acad. Sci. USA.* 82:6153–6157.

Discher, D. E., D. H. Boal, and S. K. Boey. 1998. Simulations of the erythrocyte cytoskeleton at large deformation II: micropipette aspiration. *Biophys. J.* 75:1584–1597.

Discher, D. E., and N. Mohandas. 1996. Kinematics of red cell aspiration by fluorescence-imaged microdeformation. *Biophys. J.* 71:1680–1694.

Discher, D. E., N. Mohandas, and E. A. Evans. 1994. Molecular maps of red cell deformation: hidden elasticity and in situ connectivity. *Science.* 266:1032–1035.

Discher, D. E., R. Winardi, P. O. Schischmanoff, M. Parra, J. G. Conboy, and N. Mohandas. 1995. Mechanochemistry of protein 4.1's spectrin-actin binding domain: ternary complex interactions, membrane binding, network integration, structural strengthening. *J. Cell Biol.* 130:897–907.

Evans, E. A. 1973. New membrane concept applied to the analysis of fluid shear- and micropipette-deformed red blood cells. *Biophys. J.* 13: 941–954.

Evans, E. A., and R. Skalak. 1980. Mechanics and Thermodynamics of Biomembranes. CRC Press, Boca Raton, FL.

Fowler, V. M. 1996. Regulation of actin filament length in erythrocytes and striated muscle. *Curr. Opin. Cell Biol.* 8:86–96.

Franzese, G. 2000. Potts fully frustrated model: thermodynamics, percolation, and dynamics in two dimensions. *Phys. Rev. E.* 61:6383–6391.

Hiraoka, Y., J. W. Sedat, and D. A. Agard. 1987. The use of a charge-coupled device for quantitative optical microscopy of biological structures. *Science.* 238:36–41.

Holley, M. C., and J. F. Ashmore. 1990. Spectrin, actin and the structure of the cortical lattice in mammalian cochlear outer hair cells. *J. Cell Sci.* 96:283–291.

Kas, J., H. Strey, J. X. Tang, D. Finger, R. Ezzell, E. Sackmann, and P. A. Janmey. 1996. F-actin, a model polymer for semiflexible chains in dilute, semidilute, and liquid crystalline solutions. *Biophys. J.* 70: 609–625.

Kishino, A., and T. Yanagida. 1988. Force measurements by micromanipulation of a single actin filament by glass needles. *Nature.* 334:74–76.

Landau, L. D., and E. M. Lifshitz. 1986. Theory of Elasticity, 3rd Ed. Pergamon Press, Oxford.

Lee, J. C.-M., D. Wong, and D. E. Discher. 1999. Direct measures of large, anisotropic strains in deformation of the erythrocyte cytoskeleton. *Biophys. J.* 77:853–864.

Mohandas, N., and E. Evans. 1994. Mechanical properties of the red cell membrane in relation to molecular structure and genetic defects. *Annu. Rev. Biophys. Biomol. Struct.* 23:787–818.

Mullins, R. D., J. A. Heuser, and T. D. Pollard. 1998. The interaction of Arp2/3 complex with actin: nucleation, high affinity pointed end capping, and formation of branching networks of filaments. *Proc. Natl. Acad. Sci. USA.* 95:6181–6186.

Oghalai, J. S., and A. A. Patel, T. Nakagawa, and W. E. Brownell. 1998. Fluorescence-imaged microdeformation of the outer hair cell lateral wall. *J. Neurosci.* 18:48–58.

Picart, C., and D. E. Discher. 1999. Actin protofilament orientation at the erythrocyte membrane. *Biophys. J.* 77:865–878.

Reid, M. E., Y. Takakuwa, J. Conboy, G. Tchernia, and N. Mohandas. 1990. Glycophorin C content of human erythrocyte membrane is regulated by protein 4.1. *Blood.* 75:2229–2234.

Rief, M., J. Pascual, M. Saraste, and H. E. Gaub. 1999. Single molecule force spectroscopy of spectrin repeats: low unfolding forces in helix bundles. *J. Mol. Biol.* 286:553–561.

Shen, B. W., R. Josephs, and T. L. Steck. 1986. Ultrastructure of the intact skeleton of the human erythrocyte membrane. *J. Cell. Biol.* 102: 997–1006.

Tsuji, A., K. Kawasaki, S. Ohnishi, H. Merkle, and A. Kusumi A. 1988. Regulation of band 3 mobilities in erythrocyte ghost membranes by protein association and cytoskeletal meshwork. *Biochemistry.* 27:7447–7452.

Ursitti, J. A., and V. M. Fowler. 1994. Immunolocalization of tropomodulin, tropomyosin and actin in spread human erythrocyte skeletons. *J. Cell. Sci.* 107:1633–1639.

Waugh, R. E., and P. Agre. 1988. Reductions of erythrocyte membrane viscoelastic coefficients reflect spectrin deficiencies in hereditary spherocytosis. *J. Clin. Invest.* 81:133–141.

Zhukarev, V., F. Ashton, J. M. Sanger, J. W. Sanger, and H. Shuman. 1995. Organization and structure of actin filament bundles in Listeria-infected cells. *Cell Motil. Cytoskeleton.* 30:229–246.